Acta Montanistica Slovaca
ISSN 1335-1788
actamont.tuke.sk

Identification of Rotary Axis Positioning Errors in the Machining of Mining Equipment Components Using Machine Learning Techniques

Jerzy JÓZWIK[1], Marcin BARSZCZ[2], Paweł TOMIŁO[3], Ivan KURIC[4] and Daria SAŁAMACHA[5]*

Authors' affiliations and addresses:
[1] Lublin University of Technology, Faculty of Mechanical Engineering, Department of Production Engineering, Nadbystrzycka Street 36, 20-618 Lublin, Poland
e-mail: j.jozwik@pollub.pl

[2] Lublin University of Technology, Faculty of Electrical Engineering and Computer Science, Department of Computer Science, Nadbystrzycka Street 38 A, 20-618 Lublin, Poland
e-mail: m.barszcz@pollub.pl

[3] Lublin University of Technology, Faculty of Management, Department of Marketing, Nadbystrzycka Street 38, 20-618 Lublin, Poland
e-mail: p.tomilo@pollub.pl

[4] University of Žilina, Faculty of Mechanical Engineering, Department of Automation and Production Systems, Univerzitná Street 8215/1, 010 26 Žilina
e-mail: ivan.kuric@fstroj.uniza.sk

[5] Lublin University of Technology, Faculty of Mechanical Engineering, Department of Production Engineering, Nadbystrzycka Street 36, 20-618 Lublin, Poland
e-mail: s97261@pollub.edu.pl

***Correspondence:**
Ivan Kuric, University of Žilina, Faculty of Mechanical Engineering, Department of Automation and Production Systems, Univerzitná Street 8215/1, 010 26 Žilina
e-mail: ivan.kuric@fstroj.uniza.sk

Funding information:
Lublin University of Technology
8/IP/2025/F

Acknowledgement:
The research was funded under the project Lublin University of Technology - Excellent Science: "Investing in Potential" (grant no. 8/IP/2025/F).
This work was supported by the project VEGA 1/0470/23 - "Research into methods and means of implementing artificial intelligence in automated quality control systems for products with volatile quality parameters."

How to cite this article:
Józwik, J., Barszcz, M., Tomiło, P., Kuric, I. and Sałamacha, D. (2025). Identification of Rotary Axis Positioning Errors in the Machining of Mining Equipment Components Using Machine Learning Techniques. *Acta Montanistica Slovaca*, Volume 30 (3), 759-775

DOI:
https://doi.org/10.46544/AMS.v30i3.16

Abstract
This study addresses rotary-axis positioning errors that degrade dimensional fidelity during machining of mining-equipment components – particularly conical picks and their toolholder interfaces, where press-fit sockets and conical shanks demand tight tolerances. We propose a data-driven identification framework that learns the mapping from R-Test trajectories to the worktable's rotation-center errors along X′/Y′/Z′. Experiments on two five-axis milling machines (monoBLOCK 65 and Lasertec 65) covered full 360° rotations (Δα = 30°), both directions of motion, radii R = 75–300 mm, and feeds vf = 500–5000 mm/min. After statistical analysis and feature engineering, three models were benchmarked: a multilayer perceptron (MLP), a Kolmogorov-Arnold network (KAN), and a multi-output Gaussian process (MOGP). MOGP achieved the best predictive fidelity (average R2 = 0.991, MPE = 2.29%, MSE = 0.002), outperforming KAN (R^2 = 0.974) and MLP (R^2 = 0.761). Error distributions showed weak sensitivity to feed and motion direction (left-right correlations ≥ 0.90, lowest for Z′), indicating predominantly geometric/thermal origins. The learned model enabled a high-resolution "error map" of the worktable based on resultant displacement, supporting corrective actions that preserve press-fit tolerances and free rotation in mining-component assemblies. We further implemented an integrated diagnostic tool that ingests raw R-Test exports, validates units/ranges, performs model-aware inference, and generates bilingual (PL/EN) technical reports. Embedded rule-based logic flags likely mechanisms (backlash, thermal drift, geometric misalignment) from trajectory patterns, bridging quantitative predictions with maintenance decisions. The results demonstrate that nonparametric, uncertainty-capable multi-output modeling is a robust foundation for rotary-axis error cartography and diagnostics, with immediate applicability to quality assurance and predictive maintenance in the machining of mining-equipment components.

Keywords
conical pick, manufacturing, identification of errors, CNC machine, machine learning

Introduction

Machining of mining equipment components imposes tight geometric requirements on multi-axis CNC machine tools, because dimensional fidelity at the interfaces – press-fit sockets, conical shanks, flanges, and housings – directly determines cutting-system reliability. In tangential cutting systems, conical picks are the primary cutting tools: failures at the pick-to-toolholder assembly result in lower output, higher drive loads, and unplanned downtime. Field and laboratory studies consistently highlight dominant failure modes: wear and/or chipping of the carbide tip, wear and buckling of the steel body, and accelerated destruction when free rotation is blocked in the holder socket (Cheluszka et al., 2021; Sun & Li, 2014). The assembly context and typical geometrical relationships for conical picks and auxiliary components are illustrated in Figure 1.

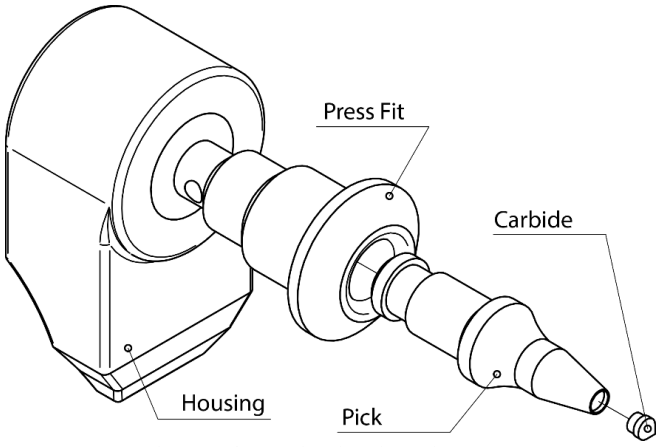

Fig. 1. Example view of conical pick with auxiliary components

Design and manufacture of the pick-holder system critically affect wear rate and uptime. Reported causes of premature failures include adverse wear mechanisms and carbide fractures, improper geometry, and loss of free rotation; by contrast, precision of the mounting components (holder bores, sockets, press-fit seats) promotes stable load sharing and reduces failure rates (Murčinková et al., 2018; Wirtgen, n.d.). Ensuring such precision depends on capable CNC machining and proper calibration of the machine's kinematic chain; for complex shank, flange, and socket geometries, five-axis accuracy is decisive in maintaining tolerances that guarantee free rotation and balanced forces under abrasive service (Guo et al., 2024; Qiao et al., 2017; Kovanič et al, 2020; Kovanic et al, 2021)

A persistent practical bottleneck is the identification of rotary-axis positioning errors. Misalignment, backlash, and thermally driven drift manifest as dimensional deviations in sockets and shanks, resulting in improper press fits and a risk of jamming or operational backlash. Studies confirm that systematic identification and compensation of rotary-axis errors improve part quality and repeatability while reducing scrap (Li et al., 2019; Zha & Peng, 2025,). Recent developments relevant to mining-component machining include high-information-density R-test (capacitive/laser) procedures that sense tri-axial deviations during coordinated motion and enable faster decoupling of position-independent and position-dependent geometric errors (PIGEs/PDGEs); transposed-matrix and constraint-aware formulations further improve robustness of parameter identification and controller-level compensation (Hsieh et al., 2024; Tang et al., 2025; Chen et al., 2025; Yao et al., 2023).

Parallel progress in machine learning (ML) expands the diagnostic and predictive toolkit for CNC error fields. Beyond point-estimate regressors, Gaussian-process regression and uncertainty-aware models provide calibrated prediction intervals suitable for confidence-bounded compensation and maintenance scheduling; reviews and applications report whole-machine thermal/geometric modeling, uncertainty-driven compensation, and real-time surrogate architectures for on-machine deployment (Jóźwik et al., 2024; Tomiło et al., 2023; Yadav et al., 2024; Mu et al., 2025; Kaftan et al., 2025; Huang et al., 2025).

This article argues that identifying CNC rotary-axis errors is a critical enabler of quality in cutting-tool assemblies for mining applications. While traditional calibration remains effective, its cost and downtime motivate data-driven approaches. Accordingly, we present an ML-based framework for reliable estimation of the geometric error field of the entire CNC machine worktable, using high-resolution R-test data to learn mappings from radius, feed, motion direction and rotation angle to the table's rotation-center errors along X′/Y′/Z′; we benchmark MLP, KAN and multi-output GPR and discuss implications for diagnostics and compensation in machining of mining equipment components.

Literature Review

Conical picks and their toolholder interfaces provide a representative case in which machining tolerances govern reliability under abrasive cutting. Prior work has identified design and process factors that improve the functional performance of conical picks (Cheluszka et al., 2021). Complementary studies on heavy-duty components – such as bearing rings and hydraulic-cylinder liners – highlight the importance of precision fits and surface integrity, consistent with the tolerance requirements of the socket-shank press fit considered here (Jouini et al., 2022; Dzyura & Maruschak, 2021; Sender & Buj-Corral, 2023). At a broader level, developments in materials processing for mining equipment – for instance, diamond-abrasive finishing of wear-resistant parts – underscore that geometric control and surface finish are key determinants of uptime and maintenance costs (Wang et al., 2025; Wen et al., 2025).

Rotary-axis error measurement and identification (5-axis CNC). For the socket and holder features of mining components, rotary-axis accuracy dominates form and positional fidelity. Beyond DBB and laser interferometry, R-test variants raise information density by sensing tri-axial deviations during coordinated motion. Laser R-test enables angular-position calibration and controller-integrated compensation, with documented accuracy gains on complex parts (Hsieh et al., 2024). Concurrently, transposed-matrix identification using laser trackers accelerates registration between tracker and machine coordinates, improving decoupling of linear/rotary error terms (Tang et al., 2025). Constraint-aware formulations enforce theoretical invariants of the R-test to stabilize transformation matrices when installation parameters drift (Chen et al., 2025). Efficient dual-five-axis procedures further compress calibration loops by combining geometric and dynamic error identification (Xu et al., 2024), while simultaneous schemes estimate PDGEs and PIGEs of dual rotary axes in a single campaign – a feature relevant to table-tilting architectures common in component finishing (Yao et al., 2023).

From identification to compensation in mining-component machining. Comprehensive reviews detail advances in geometric-error measuring/modeling and accuracy-design strategies for CNCs, providing theoretical bases for pairing R-test-derived parameters with controller compensation tables (Zhang et al., 2024; Wang et al., 2025). Influence-analysis frameworks and R-test-based identification of tilting-head/rotary-table errors (Lyu et al., 2024) support prioritization of error contributors when machining sockets and shanks with tight rotational-symmetry constraints. For productionized mining components beyond conical picks – e.g., slewing-bearing seats, flanges, hydraulic cylinder ends – these methods reduce rework and improve interchangeability.

Data-driven error modeling and uncertainty. Machine-learning methods are playing an increasingly important role in predicting thermal and geometric errors. Reviews emphasize Gaussian-process regression for accuracy and calibrated uncertainty (Mu et al., 2025), while applied studies demonstrate whole-machine GPR models (Chen et al., 2025), uncertainty-driven compensation that uses prediction intervals to gate corrections (Kaftan et al., 2025), and real-time surrogate compensation architectures that retain at least 95% of a high-capacity model's accuracy inside CNC loop constraints (Huang et al., 2025). Additional work on gradient-boosting/XGBoost and iterative screw compensation shows practical pathways to integrate learned models with mechatronic subsystems (Rong et al., 2023; Gao et al., 2024). In mining-component machining, these approaches can trigger recalibration when predictive uncertainty crosses thresholds, thereby protecting press-fit quality and free rotation in sockets even under thermal drift and tool wear.

Materials and Methods

The subject of the research were two five-axis CNC milling machines with a tilting rotary table: monoBLOCK 65 and Lasertec 65, on which measurements of the kinematic positions of the rotary axes were performed. The selection of these machine tools was dictated by the different levels of use: the monoBLOCK 65 was used cyclically for testing, while the Lasertec 65 was used periodically. The monoBLOCK 65 machine was equipped with a Sinumerik 840D control system with a maximum spindle speed of 30.000 rpm, while the Lasertec 65 was equipped with a Sinumerik 840D control system with a maximum speed of 24.000 rpm.

The study used the R-Test measurement system, consisting of a measuring head, a mandrel, and a reference ball. The head was mounted in the spindle tool holder, while the measuring ball was mounted on the machine tool table at a specified distance from the center of rotation (R). The head was equipped with three measuring transducers operating at 2.4 GHz, enabling the recording of relative deviations in the reference ball position relative to the head. A photo of the R-test system is shown in Figure 2.

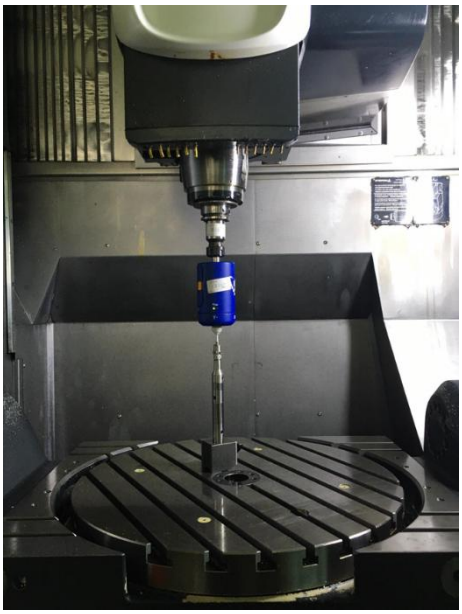

Fig. 2. The R-Test system

The measurement program controlled the interpolated movement of the machine table within a range of 360°, with a stroke angle of α = 30° and two directions of movement (right and left). Four feed speeds were used: 500, 2000, 3500, and 5000 [mm/min]. Measurements were performed for radii R = 75, 150, 225, and 300 [mm].

The results from measurements carried out on the machines presented above were used to perform statistical analyses and feature engineering, and then to develop and compare machine learning models to select the best one. As part of this article, an IT tool was also developed – an application enabling the analysis of work table errors and inference based on the selected machine learning model. The research methodology used is presented in Figure 3.

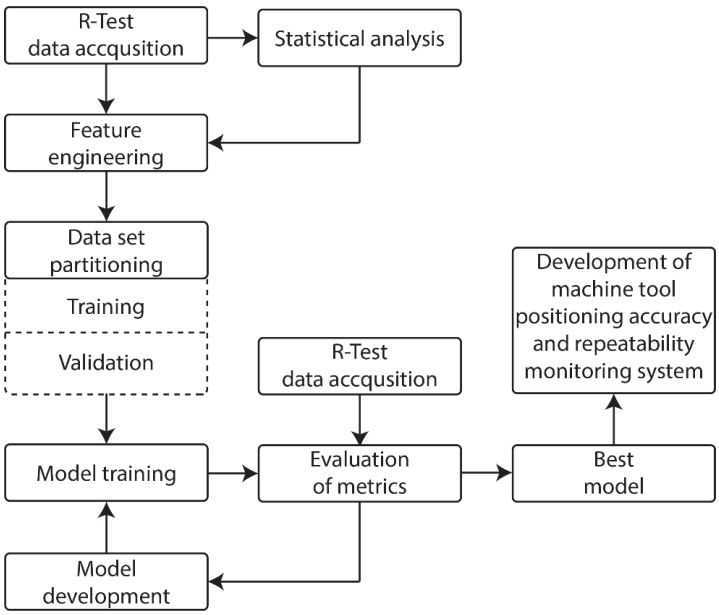

Fig. 3. Methodology of the study

In addition, a numerical analysis of the results of CNC machine tool measurements was carried out. These data were collected as the measurement radius R, feed rate vf, motion direction D, and table rotation angle α of the CNC machine tools. Then models were developed to estimate the position errors of the table's center of rotation in three linear axes designated X', Y', Z'. Statistical analysis was carried out to determine the overall difficulty of the problem. This allowed the selection of appropriate data modeling methods. To model the relationships among the described variables, 3 approaches based on a multilayer perceptron (MLP), a Kolmogorov-Arnold network (KAN), and a multi-output Gaussian process (MOGP) were considered. The models were compared using 2 mean

error (MPE) metrics and the R^2 coefficient of determination. The metrics in question are represented by equations (1) and (2):

$$MPE(y,\hat{y}) = \frac{100\%}{n}\sum_{i=1}^{n}\frac{y_i - \hat{y}_i}{y_i} \tag{1}$$

where:

n – number of samples,
y_i – i-th ground truth value,
$\hat{y}_i$ – i-th estimated value.

$$R^2(y,\hat{y}) = 1 - \frac{\sum_{i=1}^{n}(\hat{y}_i - y_i)^2}{\sum_{i=1}^{n}(y_i - \overline{y})^2} \tag{2}$$

where:

$\overline{y}$ – mean of ground truth values.

Due to the nature of the analyzed data and the possibility of complex, nonlinear relationships between input and output variables, a decision was made to develop and apply machine learning models based on three different approaches:

- Multilayer Perceptron (MLP)
- Kolmogorov-Arnold networks (KAN);
- Gaussian Process (GP).

The use of machine learning-based solutions is further justified by numerous reports in the literature indicating the high effectiveness of these methods in areas related to machine tool technology and, more broadly, in the fields of production engineering and technological process analysis, as well as in issues related to mining (Hussain et al., 2025; Kayathingal et al., 2025; Senthil et al., 2021).

MLP model

A multilayer perceptron (MLP) is one of the fundamental architectures of artificial neural networks, characterized by the presence of at least one hidden layer between the input and output layers. The presence of these additional layers enables effective modeling of complex, nonlinear relationships between input and output data, thereby significantly increasing the model's approximation capacity. The MLP structure is based on sequential signal processing by alternating layers of linear transformations, implemented using weight matrices and offset vectors (biases), and nonlinear activation functions, which introduce the nonlinearity necessary to solve classification and regression problems. MLP is a layered artificial neural network architecture, consisting of at least one hidden layer, which allows modeling complex nonlinear relationships. This type of model uses layers of linear transformations – weight matrices and nonlinear activation functions (Singh & Banerjee, 2019). The principle of a single neuron in the MLP layer is shown in equation (3):

$$y_l(x) = \phi\left(\sum_{i=1}^{n}\omega_{l,i}x_{l,i} + b_l\right) \tag{3}$$

where:

l – l-th layer;
$\phi(\cdot)$ – activation function;
x_i – i-th element of input x;
ω_i – i-th weight;
b – bias.

KAN model

Unlike multilayer perceptrons (MLPs), networks with the KAN (Kolmogorov-Arnold network) architecture do not rely on the classic alternating linear and nonlinear activation function mechanism. Instead, they use direct transformation of input values using a set of adaptive basis functions, whose shape and parameters are adjusted during the learning process. The theoretical foundation of this concept is the Kolmogorov-Arnold approximation theorem (Hou & Zhang, 2024; Liu et al., 2024; Ta, 2024). This theorem states that every continuous n-variable function defined on a compact domain (for instance, an n-dimensional cube) can be expressed as a finite combination of continuous single-variable functions and their sum. Formally, let f be any continuous function from the space R^n *in R.* Then, there exist continuous one-dimensional functions Φ_q and $\phi_{q,p}$, defined respectively for the indices p and q, such that equation (4), representing the Kolmogorov-Arnold decomposition, is satisfied. This result provides the mathematical basis for designing KAN networks, in which the learning process boils down to constructing and tuning these basis functions to map a given input-output relationship with a given approximation accuracy.

$$f(x_1, \ldots, x_n) = \sum_{q=1}^{2n+1} \Phi_q \left(\sum_{p=1}^{n} \phi_{q,p}(x_p) \right) \tag{4}$$

In KAN architecture, a key element is the construction of basis functions that enable the transformation of input data in accordance with Kolmogorov-Arnold approximation theory. In practical implementations, B-splines are used for this purpose, which are a family of basis functions defined locally on intervals. These splines ensure continuity and smoothness of a specified order at the boundaries of the intervals. The construction process begins with selecting nodes, i.e., a set of points that define the boundaries of subintervals on which individual fragments of the function are defined. The distribution of nodes determines the model's local flexibility and directly impacts the network's ability to approximate complex functions.

The value of the basis function at any point is calculated using the Cox-de Boor recursive formula – equation (5). This allows for stable and efficient determination of the values of basis functions at each point, based on the given nodes and coefficients (Ta, 2024).

$$\phi_{q,p}(x_p) = \sum_{i=0}^{n} K_{q,p,i} \cdot B_{i,k}(x_p) \tag{5}$$

where:

$B_{i,k}(x_p)$ – k-degree B-spline,
$K_{q,p,i}$ – control factor,
n – nodes number.

Gaussian Process

GPs are nonlinear, probabilistic models used to model functions and estimate values at given points. Formally, they can be treated as a generalization of the multidimensional normal distribution to an infinite-dimensional space, allowing probability distributions to be defined directly on the function space. Thanks to this, GPs not only allow the prediction of function values but also the quantification of the uncertainty associated with these predictions (Beckers, 2021; Dudek et al., 2022).

Let $f_{GP}(x)$ be a measurable function defined on the sample space with index $x \in X \subseteq R^{n_x}$, which is a random variable on this space. The a priori distribution in the Gaussian process can be fully described by the mean function $m(x)$ and the covariance function $k(x, x')$ according to equation (6):

$$f_{GP}(x) GP\big(m(x), k(x, x')\big) \tag{6}$$

For tasks requiring the simultaneous estimation of multiple output parameters, an extension of the Gaussian process, the multi-output Gaussian process (MOGP), is used. This method allows capturing relationships and similarities among output values estimated from common input parameters (Bonilla et al., 2007). For this purpose, a suitably defined covariance function is used, as shown in equation (7):

$$k([x, i], [x', j]) = k_{RBF}(x, x') * k_{out}(i, j) \tag{7}$$

where:

x – value from the data set;
x' – value from the data set with which the value x is compared.
k_{RBF} – Radial Basis Function,
k_{out} – inter-output covariance lookup table;
i, j – output indices

Dataset and feature engineering

The developed data set included 1.568 measurements of deviations of the position of the center point of the reference sphere in three linear axes, marked as X', Y', and Z'. For each measurement, the values of the input parameters were also recorded: R – radius [mm], v_f – feed rate [mm/min.], D – direction of movement, and α – angle of rotation [°]. In the initial stage of statistical analysis, basic measures of central tendency and dispersion were determined, including arithmetic mean, standard deviation, minimum and maximum values, and first (Q1), second (Q2, median), and third (Q3) quartiles. The analysis showed that parameters X' and Y' were the most variable, while parameter Z' had the lowest standard deviation, indicating a smaller spread of values relative to the mean. In addition, parameters X' and Y' showed a wider range of variability compared to parameter Z'. In the case of parameter X', the distribution of values, assessed based on the median (Q2), suggests a predominance of higher values in the upper part of the distribution. The skewness analysis showed that the distribution of deviations for the X'-axis is characterized by a slight positive skewness (0.136), which means a slight shift of the distribution towards positive values, but this effect is very weak, and the distribution can be considered close to symmetrical. For the Y'-axis, the skewness value was 0.403, indicating moderate right-sided asymmetry, i.e., a tendency for single higher positive values to occur. On the other hand, for the Z'-axis, a negative skewness of -0.753 was

obtained, which means left-skewed asymmetry – the distribution is shifted towards negative values, and the tail of the distribution is more elongated on the side of lower values. In terms of kurtosis, the parameters X' (-0.569) and Y' (-0.458) are characterized by negative kurtosis, indicating a flat (platykurtic) shape of the distribution – the values are more dispersed, and the peak of the distribution is lower and wider than in the normal distribution. In turn, the Z' parameter showed a positive kurtosis (0.844), indicating a leptokurtic distribution, characterized by a higher, more slender peak, greater concentration of values around the mean, and heavier tails. The results of the statistical analysis are presented in Table 1.

Tab. 1. Summary of the results of the statistical analysis

Numerical controlled axis	Mean [mm]	Standard deviation [mm]	Minimum [mm]	Q1 [mm]	Q2 [mm]	Q3 [mm]	Maximum [mm]	Skewness [-]	Kurtosis [-]
X'	0.011	0.019	-0.028	-0.002	0.011	0.022	0.058	0.136	-0.569
Y'	0.006	0.018	-0.029	-0.006	0.002	0.017	0.047	0.403	-0.458
Z'	0.000	0.007	-0.022	-0.003	0.001	0.004	0.017	-0.753	0.844

In the next stage of statistical analysis, the influence of the feed rate parameter (*vf*) on the distribution of deviations in the X', Y', and Z' axes was assessed. As in the previous analysis, basic statistical measures were determined along with skewness and kurtosis coefficients, with the study conducted separately for values of *vf* = 500, 2000, 3500, and 5000 mm/min. The results indicate high stability of the distributions with respect to the feed velocity – the mean values, standard deviations, and quartile ranges remained virtually unchanged across all variants. The minimum and maximum deviation values showed only slight differences, falling within very similar ranges. However, noticeable changes occurred in the area of skewness and kurtosis. For the X' and Y' axes, the skewness values were positive and remained at a comparable level (about 0.1–0.4), indicating a slight right-sided asymmetry, stable with respect to the increase in feed velocity. The Z'-axis showed negative skewness (about -0.73 to -0.79), indicating left-sided asymmetry, which was also maintained across all variants. Similarly, the kurtosis values remained consistent – negative for the X' and Y' axes - bistatic distribution shape and positive for the Z' axis - leptokurtic distribution. In summary, the vf parameter did not have a significant impact on the variability and nature of the deviation distributions. The relationships observed for skewness and kurtosis were stable regardless of the adopted velocity value. The discussed data are presented in Table 2.

Tab. 2. Summary of the results of the statistical analysis

Numerical controlled axis	v_f = 500			v_f = 2000			v_f = 3500			v_f = 5000		
	X'	Y'	Z'	X'	Y'	Z'	X'	Y'	Z'	X'	Y'	Z'
Mean [mm]	0.011	0.006	0.000	0.011	0.006	0.000	0.011	0.006	0.000	0.011	0.006	0.000
Standard deviation [mm]	0.019	0.018	0.007	0.019	0.018	0.007	0.019	0.018	0.007	0.019	0.018	0.007
Minimum [mm]	-0.028	-0.029	-0.022	-0.028	-0.029	-0.021	-0.027	-0.029	-0.021	-0.028	-0.029	-0.021
Q1 [mm]	-0.002	-0.007	-0.003	-0.002	-0.006	-0.003	-0.002	-0.006	-0.003	-0.002	-0.006	-0.003
Q2 [mm]	0.010	0.002	0.000	0.011	0.002	0.001	0.011	0.002	0.001	0.011	0.002	0.001
Q3 [mm]	0.022	0.017	0.004	0.021	0.017	0.005	0.021	0.017	0.004	0.022	0.018	0.004
Maximum [mm]	0.058	0.047	0.017	0.057	0.047	0.017	0.058	0.047	0.017	0.058	0.047	0.017
Skewness [-]	0.167	0.423	-0.741	0.135	0.406	-0.785	0.139	0.397	-0.759	0.102	0.390	-0.728
Kurtosis [-]	-0.549	-0.434	0.858	-0.570	-0.445	0.887	-0.549	-0.457	0.863	-0.592	-0.467	0.801

In order to present the data and kernel density more accurately, the data is presented using a violin plot in Figure 4.

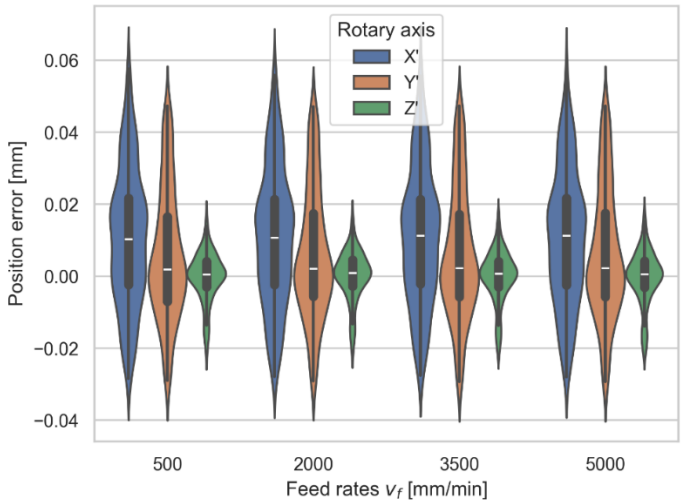

Fig. 4. Violin plot – feed rates

In the next stage of statistical analysis, the influence of the radius (R) on the distribution of deviations in the X', Y', and Z' axes was assessed. As in the case of the vf parameter, the mean values, standard deviations, ranges, and skewness and kurtosis coefficients were determined for individual radius values (R = 75, 150, 225, and 300 mm). The results indicate that the mean values and standard deviations changed only slightly with increasing radius. The greatest variation was observed for the Z'-axis, where the standard deviation increased from 0.003 mm (R = 75) to 0.011 mm (R = 300), which means a gradual increase in the spread of values. For the X' and Y' axes, the deviation values were relatively stable, with fluctuations between 0.018 and 0.020 mm. In terms of skewness, the distributions in the X' and Y' axes showed varied characteristics – from slight right-sided asymmetry (for instance, X', R = 150, skewness 0.435) to positive, more pronounced asymmetry (Y', R = 225, skewness 1.067). Negative values occurred mainly in the Z'-axis, indicating left-sided asymmetry (for instance, -0.712 for R = 300). In the case of kurtosis, all distributions had negative values, indicating a platykurtic distribution – a wider, flatter peak compared to the normal distribution. The lowest kurtosis value (-1.429) was observed for the X'-axis at R = 75, while at larger radii it ranged from -0.7 to -0.1, indicating a decrease in the flattening effect. The increase in the radius R did not significantly affect the mean and median values of the deviations, but it did increase variability along the Z' axis and reveal clear differences in the distributions' asymmetry, especially along the Y' axis. The nature of the distributions (platykurticity) remained consistent for all analyzed variants. The data discussed are presented in Table 3.

Tab. 3. Summary of the results of the statistical analysis

Numerical controlled axis	*R* = 75			*R* = 150			*R* = 225			*R* = 300		
	X'	Y'	Z'	X'	Y'	Z'	X'	Y'	Z'	X'	Y'	Z'
Mean [mm]	0.012	0.001	0.001	0.013	0.006	-0.001	0.010	0.009	-0.002	0.009	0.009	0.001
Standard deviation [mm]	0.018	0.018	0.003	0.020	0.018	0.004	0.018	0.015	0.007	0.019	0.020	0.011
Minimum [mm]	-0.016	-0.029	-0.004	-0.022	-0.017	-0.011	-0.027	-0.011	-0.020	-0.028	-0.026	-0.022
Q1 [mm]	-0.006	-0.013	0.000	0.000	-0.007	-0.003	-0.003	-0.002	-0.006	-0.004	-0.005	-0.007
Q2 [mm]	0.009	-0.001	0.001	0.011	0.001	0.000	0.014	0.002	-0.001	0.005	0.008	0.004
Q3 [mm]	0.029	0.015	0.003	0.020	0.016	0.003	0.019	0.015	0.004	0.021	0.025	0.009
Maximum [mm]	0.042	0.031	0.007	0.058	0.047	0.007	0.044	0.045	0.010	0.047	0.047	0.017
Skewness [-]	0.104	-0.035	0.156	0.435	0.959	-0.271	-0.272	1.067	-0.643	0.072	0.122	-0.712
Kurtosis [-]	-1.429	-1.145	-0.330	-0.308	-0.285	-0.689	-0.366	-0.093	-0.483	-0.738	-0.848	-0.713

In order to present the data and kernel density more accurately, the data is presented using a violin plot in Figure 5.

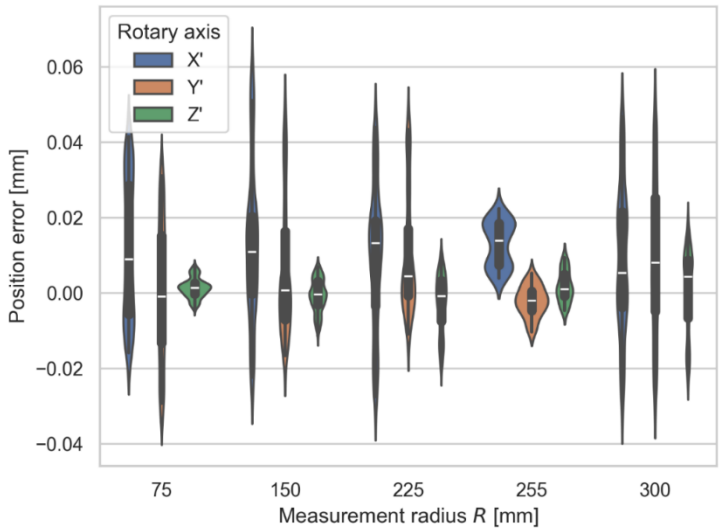

Fig. 5. Violin plot – radius

Pearson's correlation coefficient was used for feature engineering, and a correlation matrix was created based on it. The analysis was performed separately for both directions of movement – left (←) and right (→) – in relation to each axis. The main objective of the study was to determine whether the direction of movement has a significant impact on the magnitude of axial errors. The analysis showed that measurements obtained when the table rotated left and right were highly consistent. The lowest correlation coefficient recorded between movements in opposite directions, 0.9, was for the error on the Z'-axis. Such a high correlation value indicates that the direction of movement is not a significantly differentiating feature, as the errors recorded in both directions show a strong interdependence. The correlation matrix is shown in Figure 6.

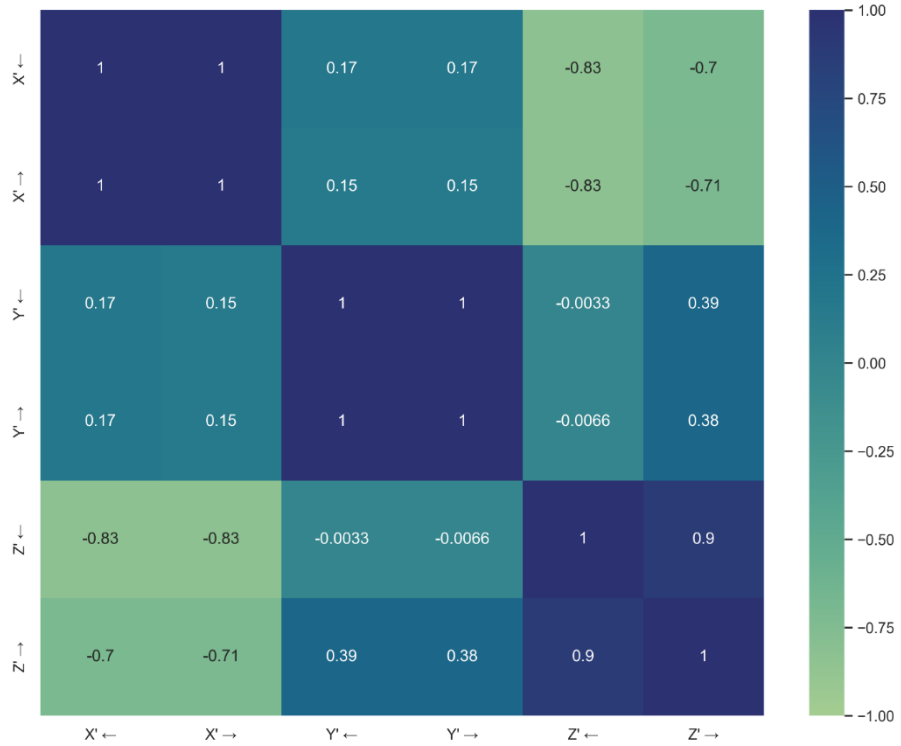

Fig. 6. Correlation matrix

Results

An artificial neural network model based on the multilayer perceptron (MLP) architecture was developed. The constructed network consisted of four input variables, two fully connected (dense) hidden layers containing 8 and 16 neurons, respectively, and three output variables. The optimization process confirmed that this architecture configuration provided the best values for the analyzed model quality assessment metrics. Mean square error

(MSE) was adopted as the loss function, while Rectified Linear Unit – ReLU was used as the activation function due to its good properties in terms of nonlinear data mapping and learning process stability. The model was trained for 100 epochs using the ADAptive Moment estimation – ADAM optimization algorithm, with the following hyperparameter settings: $\beta_1 = 0.9$, $\beta_2 = 0.999$ oraz $\epsilon = 10^{-8}$ in accordance with the recommendations in the literature (Kingma & Ba, 2014). The upper limit of the learning rate parameter was set at $\iota = 0.1$. The course of changes in the loss function value in successive epochs of the learning process is illustrated in Figure 7.

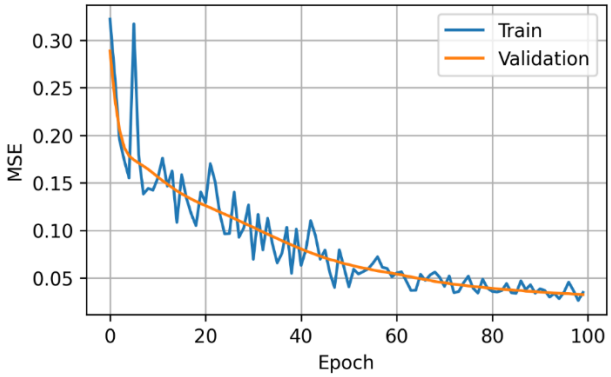

Fig. 7. Loss function – training and validation set (MLP)

The developed MLP model achieved an MSE of 0.031 on the validation set, while on the training set, it achieved 0.035. These results correspond to the hundredth epoch of the learning process, when the network achieved the best fit. For the test set, the model achieved an MPE of 14.68%, an average R^2 of 0.761, and an MSE of 0.032.

Another model was developed based on the assumptions of the KAN (Kolmogorov-Arnold network) architecture. Initially, an architecture comprising a single summing node was constructed, but its generalization ability proved insufficient. For this reason, various configurations were considered, differing in the number of layers and summing nodes. In the optimization process, an architecture consisting of a single hidden layer containing two summing nodes was ultimately selected. The input data was normalized, and the data space was defined according to Equation (8).

$$\{x \in R \vee -1 \leq x \leq 1\} \tag{8}$$

The input space was divided into 24 nodes, enabling the approximation of the function at discrete points. Twelve characteristic points were used for the approximation itself. The limited memory Broyden-Fletcher-Goldfarb-Shanno (L-BFGS) algorithm was used to optimize the network parameters (Liu et al., 2018). The model was trained for 100 epochs, with MSE as the loss function. The best metric values were obtained at the hundredth epoch, where MSE = 0.067 was achieved on the validation set, and MSE = 0.066 on the training set. The course of changes in the loss function in successive epochs of the learning process is illustrated in Figure 8.

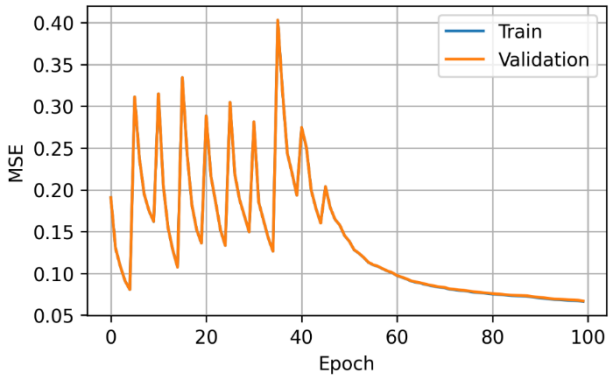

Fig. 8. Loss function – training and validation set (KAN)

On the test set, the developed model achieved an MPE of 4.86%, with a mean R2 of 0.974. An MSE value of 0.004 was also obtained, indicating very high accuracy in mapping the studied relationships. A visualization of the developed model is presented in Figure 9.

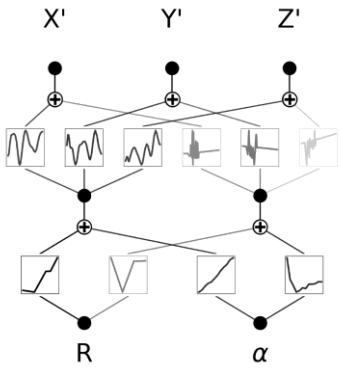

Fig. 9. Developed KAN architecture

The last model analyzed was MOGP. In this case, an accurate MOGP model consisting of a single layer was developed. The learning process was carried out using the ADAM algorithm, with the same parameters as those used in the MLP model. Marginal Log Likelihood (MLL) was adopted as the loss function, which accounts for the a priori distribution of Gaussian processes and the probability of the observed output data. This function integrates over all possible realizations of the function, enabling probabilistic modeling of relationships between data. The formal representation of the MLL function is presented in equation (9).

$$MLL(x,y) = p_f(y|x) = \int p(y \vee f_{GP}(x))p(f_{GP}(x) \vee x)df \tag{9}$$

The model underwent a learning process consisting of 100 epochs. In the hundredth epoch, the best values of the analyzed metric MLL were obtained, which amounted to -1.436 for the training set and 1.437 for the validation set, respectively. The course of changes in the loss function in successive epochs of the training process is shown in Figure 10.

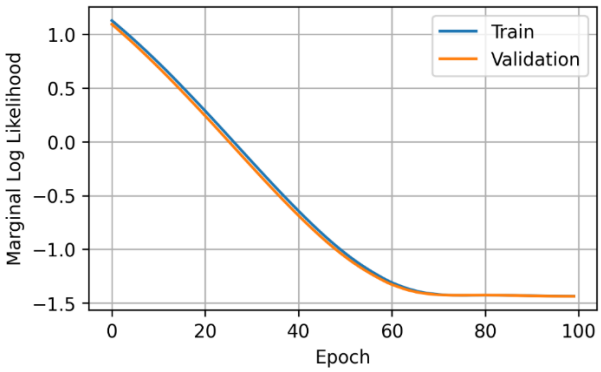

Fig. 10. Loss function – training and validation set (MOGP)

On the test set, the model achieved an average R2 of 0.991, an MPE of 2.29%, and an MSE of 0.002. Based on the research conducted, it was found that the model based on the MOGP solution achieved the best results in estimating deviation parameters. It achieved the highest values across all metrics compared with the other models analyzed, confirming its superiority in terms of accuracy and generalization. A detailed set of metric values obtained for each of the tested models is presented in Table 4.

Tab. 4. Summary of the model's metrics

	Numerical controlled axis	MOGP	KAN	MLP
R^2	X'	0.993	0.983	0.756
	Y'	0.991	0.967	0.786
	Z'	0.989	0.972	0.740
	Average	0.991	0.974	0.761
MPE, %		2.29	4.86	14.68
MSE [-]		0.002	0.004	0.032

At the final stage of the research, a map of the work table was developed, taking into account the deviation values at individual measurement points using the MOGP model. For clearer visualization of the results, the deviations along the three axes were combined into a resultant displacement, as defined in equation (10).

$$R_d = \sqrt{(X')^2 + (Y')^2 + (Z')^2} \tag{10}$$

The work table map is shown in Figure 11.

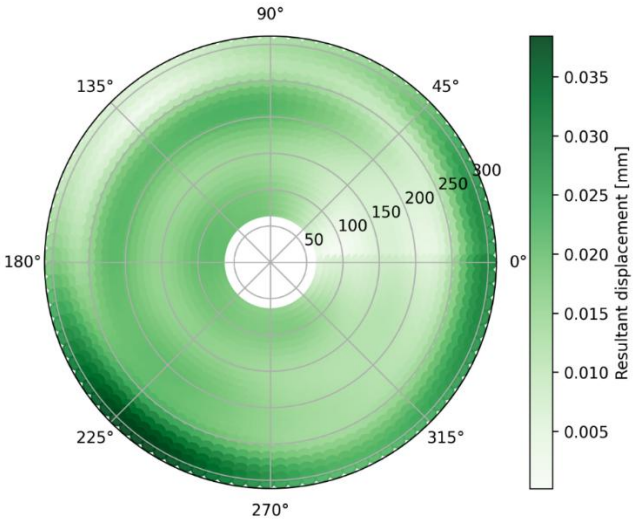

Fig. 11. Work table map

Diagnostic system – architecture and implementation

In the final phase of the study, a diagnostic system was developed that integrates previously validated machine-learning models with a procedure for analyzing error trajectories for rotary axes. The tool executes a processing pipeline from raw R-Test files to a technical report and is adapted to operate on multi-session measurement datasets. Its functional core comprises three logical components: input data preparation, inference and anomaly classification, and automatic reporting with maintenance recommendations (Figure 12). This corresponds to the role allocation of the models (MLP/KAN/MOGP) adopted in the paper for nonlinear data, as well as to the choice of evaluation metrics (R^2, MPE, MSE). In particular, the default inference configuration is MOGP, which reflects the experimentally demonstrated quality advantage over the alternatives KAN and MLP.

Fig. 12. Integrated system architecture

The system accepts text files exported from the R-Test and begins the analysis by locating the MEASUREMENT_DATA tag, which is followed by the tabular section. The parser reads columns including, among others, the angle α in degrees and the displacement components X', Y', Z', as well as auxiliary fields (time and sample indices). Merging multiple files into a single data frame is supported, allowing collation of measurements from different radii (R), feeds (vf), and both directions of motion. As a result, the tool remains

consistent with the dataset used in the statistical analysis (number of samples; features: R, v_f, D, α; outputs: X', Y', Z').

Pre-processing includes consistency validation and range checks, as well as unit harmonization and preparation of basic visualizations of displacement trajectories versus angle. At this stage, the user defines tolerance thresholds for each axis, which are then used both to mark warning levels on the plots and to perform initial qualification of exceedance cases. These settings, available from the graphical interface, are reflected immediately in the analysis and in the final report.

The inference layer provides a choice of model (MLP/KAN/MOGP) and operates in a "model-aware" mode on both axial trajectories and the worktable map. In practice, consistent with the results, MOGP is recommended as the default predictive path because it most faithfully reproduces the relationships between input features and displacements and allows a stable aggregation of the X', Y', Z' components into the resultant displacement, which is useful for error cartography of the table. A tabular record of model quality, as well as a description of the training process and hyperparameter selection (including the use of MLL for MOGP), is provided in the main results section of the manuscript and justifies the default policy adopted in the application.

Based on the X′/Y′/Z′ trajectories and their relationships to time and direction of motion, the system performs consistent diagnostics. In the first step, exceedances of the specified thresholds are checked. Next, rules are triggered to distinguish the nature of disturbances: (i) step changes in amplitude in the immediate vicinity of a direction change indicate mechanical backlash, (ii) a monotonic increase over time in the absolute values of deviations with positive correlation is interpreted as thermal drift, whereas (iii) cyclic components visible in spectral analysis suggest a geometric error (for instance, due to misalignment). The implementation of these rules was designed to align with the statistical observations from earlier sections: the minor role of motion direction (the lowest correlation between opposite directions for the Z′ axis) and the stability of distributions with respect to changes in feed vf favor the use of thresholds and heuristics with fixed parameters. In ambiguous cases, a classification of "Other" is provided, along with a glossary of explanations (also for the categories Servo/Encoder error).

A set of visualizations ties together the computational and user layers. The graphical interface (Tkinter) provides two zones: a control panel with model selection, thresholds, a language switch (PL/EN), and I/O operations; and a data presentation area with a 2×2 layout showing the $X'/Y'/Z'$ traces versus angle and the table error map (contouring based on griddata interpolation), supplemented with tabs: diagnostic results, explanations, and session history. This architecture facilitates the translation of quantitative findings (for instance, MOGP estimates) into visuals compatible with maintenance practice and industrial metrology. The main interface of the diagnostic system is shown in Figure 13.

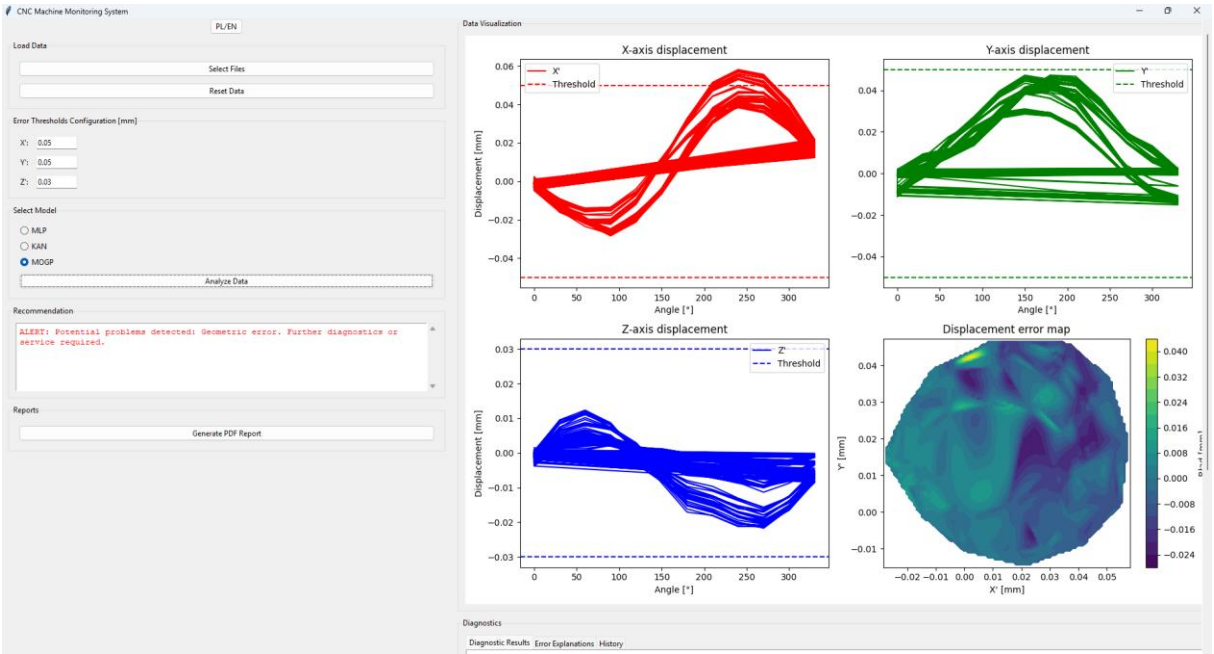

Fig. 13. View of the main interface of the diagnostic system

The reporting mechanism generates a PDF file containing a timestamp, model identification, and threshold values, a summary of per-sample statistics, and a list of identified anomalies with explanations and recommendations. The report is intended as a technical document that can be attached to the quality log and used in the predictive-maintenance cycle. Both the report contents and the warning indicators in the interface are

maintained in two language versions, which increases the tool's usefulness in international environments. Examples of selected report results are shown in Figure 14.

It is important that the adopted implementation remains substantively consistent with the analysis results presented in the paper. First, the default MOGP preference in the application reflects the quality ranking in the results section. Second, the diagnostic layer respects the empirically observed stability with respect to direction of motion and feed, so that thresholds and rules do not require complex parameterization dependent on these variables. Third, the use of a table map based on resultant displacement corresponds to the method of aggregating deviations adopted in the experimental section (which facilitates the chain "model results → error-map panel → diagnostic conclusion").

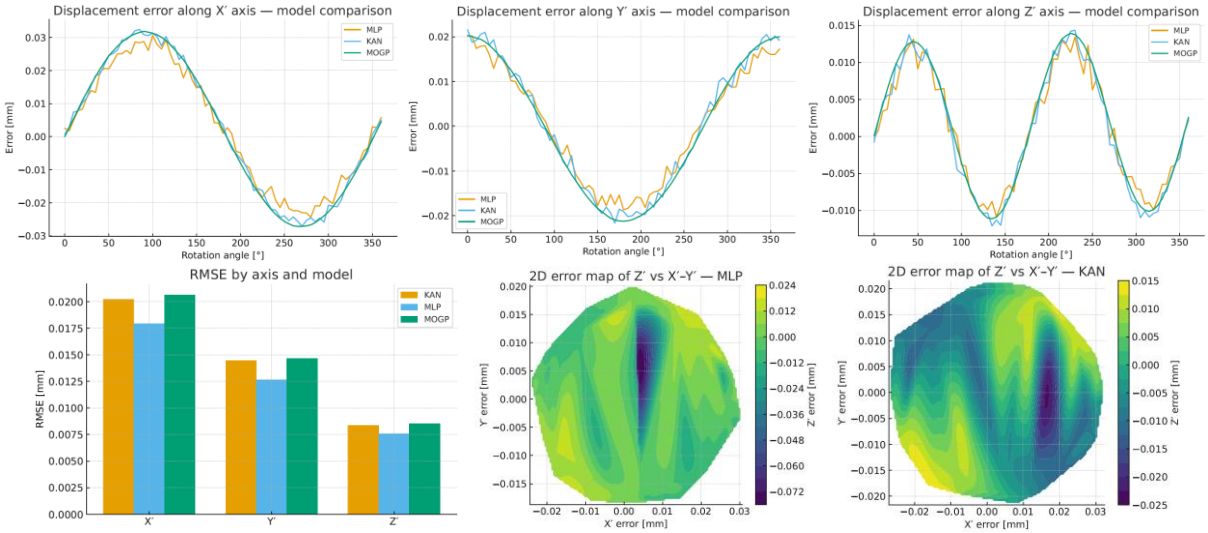

Fig. 14. Sample report results

From a technical standpoint, the solution was implemented in Python, using libraries for data processing and visualization and GUI modules; spatial interpolation in the error map is based on griddata, and document export on the FPDF component. The code implements a bilingual label dictionary, multi-file handling, and a persistent session history, which enables reproducibility and auditability of results. Extending the diagnostic functions with classes such as "servo" or "encoder" remains an open line of work and can be incorporated into the algorithm on the basis of additional, targeted datasets.

Discussion

Our results show that a multi-output Gaussian process (MOGP) most accurately reconstructs the rotary-axis error field from R-Test trajectories, achieving the best aggregate performance (average $R^2 = 0.991$, MPE = 2.29%, MSE = 0.002) and outperforming both KAN and MLP, while the measured error distributions exhibit weak sensitivity to feed v_f and motion direction (high left-right correlation, lowest for $Z' \approx 0.90$). These findings indicate that the observed deviations have a predominantly geometric/thermal rather than dynamic origin and are consistent with the statistical trends reported earlier in the manuscript.

Contemporary R-test–based procedures increase information density by capturing tri-axial deviations during coordinated motion and have been used to drive controller-level compensation (Hsieh et al., 2024). Transposed-matrix identification with external metrology improves coordinate registration and separates linear and rotary terms (Tang et al., 2025), while constraint-aware formulations stabilize parameter estimation under installation drift (Chen et al., 2025). Simultaneous schemes for dual rotary axes (Yao et al., 2023) and efficient dual-five-axis routines that combine geometric and dynamic errors (Xu et al., 2024) further reduce calibration time. Our contribution complements these methods: instead of estimating a fixed parametric set for a specific kinematic error model, MOGP learns a nonparametric, correlated multi-output mapping from (R, v_f, D, α) to (X', Y', Z'). This yields high-fidelity surface predictions and a worktable "error map" without additional hardware or complex tracker registrations, and it exploits cross-axis covariance that parametric pipelines often ignore.

Reviews of geometric/thermal accuracy design for CNCs emphasize model structures that handle nonlinearity and uncertainty (Zhang et al., 2024; Wang et al., 2025). In data regimes with moderate sample sizes and correlated targets, Gaussian-process models typically offer superior inductive bias and calibrated generalization (Mu et al., 2025), which aligns with the observed MOGP advantage. KAN, grounded in Kolmogorov-Arnold approximation, provides flexible basis functions and performed strongly here, yet it lacks the native uncertainty and cross-output covariance modeling of MOGP (Hou & Zhang, 2024; Liu et al., 2024). MLP underperformed – consistent with

prior observations that generic feed-forward networks require more data and careful regularization to match GPs on smooth, structured mappings (Singh & Banerjee, 2019). Together, this ranking mirrors trends in thermal/geometric error prediction where GP-based models or uncertainty-aware surrogates frequently lead (Huang et al., 2025; Kaftan et al., 2025; Rong et al., 2023; Gao et al., 2024).

For conical picks and toolholder interfaces, dimensional fidelity of sockets and shanks governs free rotation, load sharing, and wear rate under abrasive cutting (Cheluszka et al., 2021; Sun & Li, 2014). Mounting-component precision is a documented lever on reliability (Murčinková et al., 2018) and is also reflected in OEM guidance for quick-change systems (Wirtgen, n.d.). By reducing unmodeled rotary-axis positioning errors through accurate estimation and map-based visualization, our approach directly supports maintaining press-fit tolerances and surface integrity that downstream studies link to uptime (Jouini et al., 2022; Sender & Buj-Corral, 2023). The weak dependence on v_f and motion direction observed here suggests that, for finishing of sockets/shanks and similar rotationally constrained features, compensation efforts should prioritize geometric and thermal sources – consistent with recent influence-analysis and R-test identification frameworks for tilting-head/rotary-table architectures (Lyu et al., 2024; Guo et al., 2024; Qiao et al., 2017).

Surveys highlight that the most effective pipelines pair high-information measurements with controller tables and continuous monitoring (Zhang et al., 2024; Wang et al., 2025). Our integrated tool operationalizes this concept: it ingests raw R-Test exports, standardizes units, applies model-aware inference, and outputs a bilingual, maintenance-ready report. Probabilistic outputs typical for GPs could be extended to uncertainty-gated compensation (Kaftan et al., 2025) or to real-time surrogates (Huang et al., 2025), closing the loop between diagnostics and action.

Conclusions

Based on experimental tests and numerical analyses, a very high correlation between error values and movement direction was demonstrated, with a correlation coefficient of 0.9 for the Z-axis only. Statistical analysis also confirmed that the feed rate parameter vf had only a marginal effect on the variability of machine tool axial errors. Among the machine learning models used, the best results were obtained with the MOGP model, which achieved an average R^2 of 0.991, MPE of 2.29%, and MSE of 0.002. For comparison, the KAN model achieved an average R^2 of 0.974, while the MLP model achieved an R^2 of 0.761; both alternative approaches exhibited significantly higher errors. These results are significant for the production of components for mining machines, particularly conical pick blades and their holders. The precision of manufacturing these parts, especially the shanks and holder sockets, is crucial to ensure free rotation of the tool during operation and its even wear under highly abrasive conditions. Even slight positioning errors of the CNC rotary axes can result in geometric deviations, leading to increased friction, jamming, or premature damage to the picks during mining shearers' operation.

The developed integrated system for monitoring the accuracy and repeatability of multi-axis machine tool positioning, based on machine learning methods, has proven to be an effective diagnostic tool in laboratory conditions. It consists of three modules responsible for data processing, anomaly detection, and diagnostic report generation. The implementation of this type of system in industrial conditions, e.g., in plants producing mining tools, enables the prediction of machine tool component wear and the stable maintenance of geometric tolerances, which directly translates into higher quality and durability of the conical pick produced.

One of the most important advantages of the developed solution is its practical usefulness. The combination of modern measurement systems with modules based on artificial intelligence not only enables effective control of the technical condition of machine tools, but also bridges the gap between the theoretical approach and the real needs of the mining industry. A certain limitation of the presented methodology remains the inability to directly record data from the R-Test system in the CNC controller, which hinders the full integration of the diagnostic procedure with the native control system of the machine tool.

References

Beckers, T. (2021). An introduction to Gaussian process models. *arXiv*. https://arxiv.org/abs/2102.05497

Bonilla, E. V., Chai, M. A., & Williams, C. K. I. (2007). Multi-task Gaussian process prediction. *Advances in Neural Information Processing Systems*, *20*.

Cheluszka, P., Mikuła, S., & Mikuła, J. (2021). Conical picks of mining machines with increased utility properties – Selected construction and technological aspects. *Acta Montanistica Slovaca*, *26*(2), 195–204. https://doi.org/10.46544/AMS.v26i2.02

Chen, G., Zhou, B., Li, T., Mao, J., Li, B., & Fu, Z. (2025). Research on thermal error compensation modeling for the machine tool integrated drive system based on energy consumption big data and an optimized bidirectional network. *Precision Engineering*, *94*, 91–112. https://doi.org/10.1016/j.precisioneng.2025.02.024

Chen, H., Hu, X., Liu, Y., Tan, F., & Liao, Q. (2025). Geometric errors identification of machine tool rotary axes considering R-test theoretical model constraints. *Discover Applied Sciences*, *7*, 323. https://doi.org/10.1007/s42452-025-06807-7

Dudek, A., Baranowski, J., Liu, H., Li, J.-B., Li, M., Chen, S.-H., & Baranowski, J. (2022). Gaussian processes for signal processing and representation in control engineering. *Applied Sciences*, *12*(10), 4946. https://doi.org/10.3390/app12104946

Dzyura, V., & Maruschak, P. (2021). Optimizing the formation of hydraulic cylinder surfaces, taking into account their microrelief topography analyzed during different operations. *Machines*, *9*(6), 116. https://doi.org/10.3390/machines9060116

Gao, X., Zhang, K., Zhang, Z., Wang, M., Zan, T., & Gao, P. (2024). XGBoost-based thermal error prediction and compensation for ball screws. *Proceedings of the Institution of Mechanical Engineers, Part B: Journal of Engineering Manufacture*, *1–2*, 151–163. https://doi.org/10.1177/09544054231157110

Guo, S., Si, Z., Sa, R., Zou, Y., & Mei, X. (2024). Geometric error modeling and decoupling identification of rotary axis of five-axis machine tool based on spatial trajectory planning. *Measurement*, *236*, 114887. https://doi.org/10.1016/j.measurement.2024.114887

Hou, Y., & Zhang, D. (2024). A comprehensive survey on Kolmogorov-Arnold networks (KAN). *arXiv*. http://arxiv.org/abs/2407.11075

Hsieh, T.-H., Jywe, W.-Y., Zeng, J.-J., Hsu, C.-M., & Chang, Y.-W. (2024). Geometric error compensation method using the laser R-test. *The International Journal of Advanced Manufacturing Technology*, *31*, 4035–4053. https://doi.org/10.1007/s00170-024-13099-5

Huang, Y., Hong, H., Zhou, H., Xiang, H., & Yang, J. (2025). Real-time surrogate compensation architecture for machine-tool thermal error compensation with high-performance model. *Discover Applied Sciences*, *7*(8). https://doi.org/10.1007/s42452-024-06389-w

Hussain, J., Ali, N., Chen, J., Ahmed Khan, N., & Hussain, S. (2025). Leveraging artificial neural networks to predict igneous rock strength parameters from petrological contents. *Acta Montanistica Slovaca*, *30*(2), 470–491. https://doi.org/10.46544/AMS.v30i2.16

Jouini, N., Revel, P., & Thoquenne, G. (2022). Investigation of surface integrity induced by various finishing processes of AISI 52100 bearing rings. *Materials*, *15*(10), 3710. https://doi.org/10.3390/ma15103710

Jóźwik, J., Zawada-Michałowska, M., Kulisz, M., Tomiło, P., Barszcz, M., Pieśko, P., & Cybul, K. (2024). Modeling the optimal measurement time with a probe on the machine tool using machine learning methods. *Applied Computer Science*, *20*(2), 43–59. https://doi.org/10.35784/ACS-2024-15

Kaftan, P., Mayr, J., Porquez, F., Pomodoro, K., Trombert, D., Wegener, K., & Bambach, M. (2025). Reducing thermal errors with confidence: Uncertainty-based compensation. *CIRP Journal of Manufacturing Science and Technology, 54*, 400–409. https://doi.org/10.1016/j.cirpj.2025.06.001

Kayathingal, H., Vochozka, M., & Rowland, Z. (2025). Optimizing precious metal price forecasting with hybrid deep learning models: An operational research perspective. *Acta Montanistica Slovaca*, *30*(1), 1–16. https://doi.org/10.46544/AMS.v30i1.01

Kingma, D. P., & Ba, J. (2014). Adam: A method for stochastic optimization. *International Conference on Learning Representations (ICLR)*. https://arxiv.org/abs/1412.6980

Kovanic, L., Ambrisko, L., Marasova, D., Blistan, P., Kasanicky, T., Cehlar, M. (2021). Long-Exposure RGB Photography with a Fixed Stand for the Measurement of a Trajectory of a Dynamic Impact Device in Real Scale. Sensors, 21(20). DOI 10.3390/s21206818

Kovanič, Ľ., Blistan, P., Urban, R., Štroner, M., Pukanská, K., Bartoš, K., & Palková, J. (2020b). Analytical Determination of Geometric Parameters of the Rotary Kiln by Novel Approach of TLS Point Cloud Segmentation. Applied Sciences, 10(21), 7652. https://doi.org/10.3390/app10217652.

Li, C., Liu, X., Li, R., Wu, S., & Song, H. (2019). Geometric error identification and analysis of rotary axes on five-axis machine tool based on precision balls. Applied Sciences, 10(1), 100. https://doi.org/10.3390/app10010100

Liu, X., Liu, S., Sha, J., Yu, J., Xu, Z., Chen, X., & Meng, H. (2018). Limited-memory BFGS optimization of recurrent neural network language models for speech recognition. *Proceedings of the IEEE International Conference on Acoustics, Speech and Signal Processing (ICASSP)*, 6114–6118. https://doi.org/10.1109/ICASSP.2018.8461550

Liu, Z., Wang, Y., Vaidya, S., Ruehle, F., Halverson, J., Soljačić, M., & Tegmark, M. (2024). KAN: Kolmogorov–Arnold networks. *arXiv*. https://arxiv.org/abs/2404.19756

Lyu, D., Zhang, J., Wang, J., Liu, H., & Guo, J. (2024). R-test – based identification method for geometric errors of dual rotary axes with a tilting head and rotary table. *Measurement*, *225*, 113932. https://doi.org/10.1016/j.measurement.2023.113932

Mu, S., Yu, C., Lin, K., Lu, C., Wang, X., Wang, T., & Fu, G. (2025). A review of machine learning-based thermal error modeling methods for CNC machine tools. *Machines*, *13*(2), 153. https://doi.org/10.3390/machines13020153

Murčinková, Z., Baron, P., & Pollák, M. (2018). Study of the press fit bearing – shaft joint dimensional parameters by analytical and numerical approach. *Advances in Materials Science and Engineering*, *2018*, 2916068. https://doi.org/10.1155/2018/2916068

Qiao, Y., Chen, Y., Yang, J., & Chen, B. (2017). A five-axis geometric errors calibration model based on the common perpendicular line (CPL) transformation using the product of exponentials (POE) formula. *International Journal of Machine Tools and Manufacture*, *118–119*, 49–60. https://doi.org/10.1016/j.ijmachtools.2017.04.003

Rong, R., Zhou, H., Huang, Y., Yang, J., & Xiang, H. (2023). Real-time compensation for ball-screw thermal error. *Applied Sciences*, *13*(5), 2833. https://doi.org/10.3390/app13052833

Sender, P., & Buj-Corral, I. (2023). Influence of honing parameters on the quality of the machined parts and innovations in honing processes. *Metals*, *13*(1), 140. https://doi.org/10.3390/met13010140

Senthil, A. M. S., Muthukannan, J., Urbański, M., Stępień, M., & Kądzielawski, M. (2021). MSCA-based deep recurrent neural network for statistics risk management in construction projects. *Acta Montanistica Slovaca*, *26*(3), 481–497. https://doi.org/10.46544/AMS.v26i3.08

Singh, J., & Banerjee, R. (2019). A study on single and multilayer perceptron neural network. *Proceedings of the 3rd International Conference on Computing Methodologies and Communication (ICCMC 2019)*, 35–40. https://doi.org/10.1109/ICCMC.2019.8819775

Sun, Y., & Li, X. S. (2014). Ineffective rock breaking and its impacts on pick failures. *Proceedings of the 31st International Symposium on Automation and Robotics in Construction and Mining (ISARC)*, 754–760. https://doi.org/10.22260/ISARC2014/0102

Ta, H.-T. (2024). BSRBF-KAN: A combination of B-splines and radial basis functions in Kolmogorov-Arnold networks. *arXiv*. https://arxiv.org/abs/2406.11173

Tang, Y., Wan, Y., Ji, S., Xia, Y., & Liang, X. (2025). Measurement and identification of geometric errors in five-axis machine tools based on transposed matrix. *The International Journal of Advanced Manufacturing Technology*. https://doi.org/10.1007/s00170-025-16692-4

Tomiło, P., Pytka, J., Jóźwik, J., Gnapowski, E., Muszyński, T., & Łukaszewicz, A. (2023). Latent neural network for recognition of anomalies in 3D-print of a scale model for wind tunnel measurements. *Proceedings of the 2023 IEEE 10th International Workshop on Metrology for Aerospace (MetroAeroSpace)*, 688–692. https://doi.org/10.1109/METROAEROSPACE57412.2023.10190049

Wang, B., Chu, H., Song, C, Zhang, Q., & Zhang, H. (2025). Characteristics and mechanism of diamond abrasive grains wear under NMQL assisted grinding of SiCf/SiC composites. *Diamond and Related Materials*, *158*, 112616. https://doi.org/10.1016/j.diamond.2025.112616

Wang, L., Han, J., Tang, Z., Zhang, Y., Wang, D., & Li, X. (2025). Geometric accuracy design of high performance CNC machine tools: Modeling, analysis, and optimization. *Chinese Journal of Mechanical Engineering*, *38*, 87. https://doi.org/10.1186/s10033-025-01258-y

Wen, D., Wan, L., Zhang, X., Li, C., Ran, X., & Chen, Z. (2025). Grinding performance evaluation of SiC ceramic by bird feather-like structure diamond grinding wheel. *Journal of Manufacturing Processes*, *95*, 382–391. https://doi.org/10.1016/j.jmapro.2023.04.024

Wirtgen Group. (n.d.). Quick-Change Toolholder System HT22 PLUS HD. https://www.wirtgen-group.com/en-us/products/wirtgen/technologies/cutting-technology/toolholder-systems/ht22-recyclers/ (Retrieved October 4, 2025)

Xu, K., Zhuang, Z., Ji, Y., Xu, J., Yu, Y., & Bi, Q. (2024). An efficient method for measuring and identifying geometric and dynamic errors in dual five-axis machine tools. *Precision Engineering*, *86*, 359–375. https://doi.org/10.1016/j.precisioneng.2024.01.002

Yadav, D. K., Kaushik, A., & Yadav, N. (2024). Predicting machine failures using machine learning and deep learning algorithms. *Sustainable Manufacturing and Service Economics*, *3*, 100029. https://doi.org/10.1016/j.smse.2024.100029

Yao, S., Huang, H., Tian, W., Gao, W., Weng, L., & Zhang, D. (2023). Simultaneous identification for geometric error of dual rotary axes in five-axis machine tools. *Measurement*, *220*, 113368. https://doi.org/10.1016/j.measurement.2023.113368

Zha, J., & Peng, X. (2025). Geometric error identification and compensation of swiveling axes based on additional rotational rigid body motion constraints. *Chinese Journal of Mechanical Engineering (English Edition)*, *38*(1), 1–23. https://doi.org/10.1186/s10033-025-01221-x

Zhang, Z., Jiang, F., Luo, M., Wu, B., Zhang, D., & Tang, K. (2024). Geometric error measuring, modeling, and compensation for CNC machine tools: A review. *Chinese Journal of Aeronautics*, *37*(2), 163–198. https://doi.org/10.1016/j.cja.2023.02.035